72nd Conference of the Italian Thermal Machines Engineering Association, ATI2017, 6-8 September 2017, Lecce, Italy

Optimization of Plasma Actuator Excitation Waveform and Materials for Separation Control in Turbomachinery

E. Pescini[a],*, A. Suma[a], M. G. De Giorgi[a], L. Francioso[b], A. Ficarella[a]

[a]Department of Engineering for Innovation, University of Salento, Via per Monteroni, 73100 Lecce, Italy
[b] Institute for Microelectronics and Microsystems - CNR–IMM, Via per Monteroni, 73100 Lecce, Italy

Abstract

Different input waveforms applied to a Single Dielectric Barrier Discharge Plasma Actuator (SDBDPA) were compared for flow separation control on low-pressure turbines (LPTs). The investigated Reynolds number (*Re*) was $2 \cdot 10^4$. The work aim was the device optimization in terms of materials and excitation conditions for enhancing its durability and performances. The SDBDPA was manufactured by microfabrication techniques. Device materials that could withstand the plasma environment were selected. Sine, square and triangle waveforms were compared in terms of actuator dissipated power and induced velocity. At comparable peak-to-peak applied voltage, the sinus outperformed the other waveforms, while the square dissipated the most.

Keywords: Plasma actuator; Dielectric barrier discharge; Excitation waveform; Electrical characterization; Momentum coefficient.

1. Introduction

LPT blades subjugated to low *Re* flow effects, due to the change in density from high altitude operation, may experience laminar boundary layer separation on the suction surface together with the appearance of secondary flows [1]. The low *Re* condition becomes even a greater issue when dealing with modern high-lift blades [2] and small/medium-sized gas turbines [3], [4].
Laminar flow separation was experimentally [3] and numerically [5] observed in a single stage axial-flow turbine,

* Corresponding author. Tel.: +390832 297783.
  E-mail address: elisa.pescini@unisalento.it

operating at a *Re* (based on the stator chord length and stator inlet velocity) equal to 20.000 and an inlet turbulence intensity of 0.5%. Moreover, it was also found a strong interaction of the separated flow with the secondary flows. Similar experimental investigations under the same operating conditions were also performed in Matsunuma *et al*. [6]. Secondary flows usually cause almost 30-50% of the overall loss in a blade row with a significant reduction of the LPT efficiency [7]. Moreover, a nearly 300% increase in the loss coefficient was indicated at a *Re* below $2 \cdot 10^5$, primarily associated with a laminar separation over the trailing half of the blade suction surface [8]. Hence, the control of laminar separation bubbles has been subject of many studies in recent years.

Several flow control techniques have been investigated with particular interest in active flow control methods [9]–[11]. Among active flow control devices an interesting one is the SDBDPA, which is easy to be implemented on a surface, light in weight and with electrical input energy that allows easy control and modulation of the actuation.

The SDBDPAs are composed of two metallic electrodes separated by a dielectric layer: one electrode is supplied with a high voltage (HV) waveform and exposed to the surrounding flow; the other one is grounded and covered by insulating material. The application a voltage waveform in the kV and kHz ranges (with or without modulation or pulsing) causes the ionization of the air near the plasma actuator. The electric field's interaction with the charged particles results in a net body force that acts on the neutrally charged air. When operating in a separated flow, the body force effect leads to the energization of the boundary layer, which can results in its reattachment.

Plasma actuators have been already investigated as an effective active control strategy in eliminating the LPT separation at low *Re* [1], [8], [11]–[13]. However, these devices exhibit low electrical-to-fluidic energy conversion efficiency. Among the parameters improving the effectiveness of the SDBDPAs, it is established that the geometry of the actuator, the number of electrodes and the electric settings can significantly enhance the force production, and consequently, the resulting electric wind velocity [14].

In Bernard and Moreau [15], the influences of different waveforms (sine, square, positive and negative ramps) as input for a SDBDPA were experimentally investigated and compared in quiescent conditions. Results showed that the sine waveform was recommended as input voltage to optimize the actuators use in terms of mean force by electrical power consumption. Nevertheless, at constant applied voltage or frequency, the square signal caused higher thrust, but with high consumed power. A second metric that determines the effectiveness of such actuator for control is the mean velocity of the electric wind produced by the plasma, as well as the amplitude of the velocity fluctuations that can be achieved. Always in Bernard and Moreau [15] the largest mean flow velocity, at constant applied voltage and frequency, was observed for a square input waveform; this agreed with the force measurements. The sine waveform led to a slightly smaller mean flow velocity when performances were further degraded by using the ramp shapes (especially the positive one). However, the largest fluctuations in the velocity component in the horizontal direction (i.e., direction of the plasma layer) were observed for a sine waveform when they were minimized by using a positive ramp. This suggested that sine waveform could be probably more effective in flow separation control. Again, the amplitude of vertical velocity fluctuations was increased by using a sine waveform.

In Jolibois and Moreau [16], the waveform of the applied voltage (sine, triangle, square, trapezium, positive and negative ramps) has also been investigated as input parameter able to influence the actuator electromechanical performance, always in quiescent environment. Results showed that at same electrical power consumption, the discharge induced the same maximum velocity whatever the waveform, excepted with the square and the positive ramp ones that resulted in a smaller electric wind velocity. Comparing sinus and square, it was found that, at similar power consumption, the sine voltage induced a faster electric wind with a discharge closer to the wall than the square waveform.

In the previously cited works [15], [16] and in further available literature studying the influence of the HV waveforms [17], [18], the investigations were performed with SDBDPAs always placed in initially quiescent flow conditions. Hence, in order to verify the influence of the excitation waveform in presence of flow separation, in the present paper the LPT separation control was experimentally studied for three different voltage waveforms (sine, square and triangle). In particular, the LPT rotor investigated in the works of Matsunuma *et al.* [6], [19], [20] was considered. The applied voltage and the discharge current were acquired in order to determine the device dissipated power. Simultaneously, two-dimensional (2-D) flow velocity measurements –with and without actuation– were carried out by particle image velocimetry (PIV).

Together with the waveform optimization, in the current work the SDBDPA manufacturing procedure and materials were carefully chosen, as both influence the actuators performances and also their durability [21], [22]. Aiming to develop efficient, reproducible and durable devices, optical lithography technique was adopted. Houser et al. [22] showed the advantages in using photolithographic techniques for depositing thin electrodes with high manufacturing

reliability and control. Moreover, Houser et al. [22] and Pescini et al. [21] found that alkali-free borosilicate glass based devices did not present obvious sign of dielectric degradation in plasma environment. Copper and tungsten (W) actuator electrodes were also compared in [22] and it was showed that while the former exhibited appreciable degradation along the plasma-forming edge after usage, the latter presented limited degradation. Therefore, thin Schott AF-32 alkali-free borosilicate glass dielectric material was here selected onto which thin W electrodes were deposited. In order to enhance the lifetime of the SDBDPA by limiting the exposed electrode damage, a surface coating of the W electrodes with sputtered titanium nitride (TiN) has been also performed; Titanium (Ti) was used as adhesion layer (10 nm). The TiN is a well known wear resistant film widely adopted by the industry for coating of high speed steel tools and it was applied for the first time to SDBDPA electrodes in the current paper.

Nomenclature

c	length of the curved wall, m.	*Greek letters*	
c_μ	steady 2-D momentum coefficient.	ρ	fluid density, kg/m^3.
f	applied voltage frequency, kHz.	$\phi(t)$	applied voltage signal, V.
$I(t)$	measured current signal, A or mA.	ϕ_{pp}	peak-to-peak applied voltage, kV.
J	steady 2-D wall jet momentum, Kg/s^2.	*Subscripts*	
N	number of measurements for averaging.	*on*	quantity evaluated with actuator on.
$\overline{P}$	electrical power dissipation, W.	*off*	quantity evaluated with actuator off.
Re	Reynolds number.	*rms*	root-mean-square.
T	time period, s.	W	profile wall.
t	time instant, s.	x	x Cartesian component.
Tu	turbulence intensity, %.	y	y Cartesian component.
$\mathbf{v}$	velocity vector, m/s.	∞	variable evaluated at the freestream.
v_i	time-averaged velocity i-component, m/s.	*Superscripts*	
(x, y, z)	Cartesian coordinate system, m.	*in*	quantity evaluated at the test section inlet.
		'	fluctuation.

---

2. Experimental procedure

2.1. Actuator fabrication procedure

The actuator manufacturing was carried out at the National Research Council Institute for Microelectronics and Microsystems (CNR-IMM) in Lecce. The deposition layers and their thicknesses are reported in Fig. 1 (left). A cross-sectional view of the SDBDPA, along with its geometrical parameters dimensions, is depicted in Fig. 1 (right). The actuator backside electrode (denoted as "grounded electrode" in Fig. 1) and the AF-32 dielectric were flush mounted at the wall of the profile, whereas the upper electrode (denoted as "exposed electrode" in Fig. 1) emerged from the surface and was exposed to the surrounding air flow. Both electrodes had a spanwise length of 30 mm.
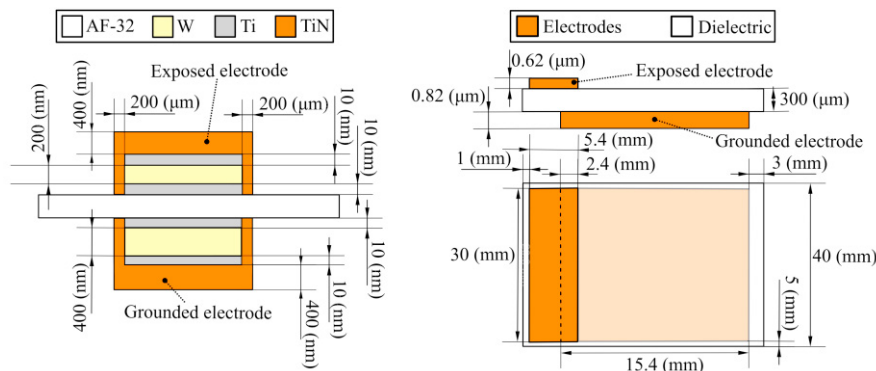

Fig. 1. Deposition layer thicknesses (left); Actuator geometry and dimensions (right).

2.2. Actuator operation and diagnostics

The flow field in presence and absence of actuation was experimentally investigated in a closed loop wind tunnel with a 120 mm x 120 mm x 840 mm test section. All acquisitions were performed at approximately 294 K and 1 bar. The SDBDPA was mounted in a curved wall plate, designed to simulate the separated flow on the suction surface of a turbine rotor blade [11] and installed in the test section of the wind tunnel. The plate profile was characterized by a streamwise (along the x-direction) length c equal to 100 mm and a spanwise (along the z-direction) length equal to 115 mm. An inlet guide wall (streamwise length equal to 56.5 mm and spanwise length equal to 115 mm) was connected to the curved wall plate. The wind tunnel had a centrifugal blower at the suction, which was driven by a frequency controller to obtain the required freestream velocity. The time averaged free stream velocity at the wind tunnel inlet (x=-86 mm) $v_{\infty,x}^{in}$ was set at 3 m/s. The Re based on the $v_{\infty,x}^{in}$ and c values was $2 \cdot 10^4$. The profile design-surface velocity distribution was derived by Matsunuma and Segawa [1] from an inviscid calculation at the midspan of the blade of the turbine rotor installed in the annular turbine wind tunnel at the National Institute of Advanced Industrial Science and Technology [6], [19], [20]. The shape of the curved wall was designed using a simple one-dimensional continuity argument to match the design-surface velocity and pressure distribution of the corresponding turbine blade. Fig. 2 shows the curved wall plate with the SDBDPA allocated, along with the adopted x-y Cartesian coordinate system. A magnified view of the SDBDPA geometry is also depicted. The origin of the x-coordinate corresponds to the minimum passage area x-location and, for each x-coordinate, the origin of the y-coordinate follows the curved wall plate. The plasma actuator was placed in a groove made in the middle of the curved wall plate, at the front of the adverse pressure gradient region (deceleration/separation region). In particular, a 1 mm dielectric rim was left before the starting of the exposed electrode (see Fig. 1 right), in order to avoid unwanted arching between the exposed and grounded electrodes. Therefore, the actuator glass layer began at x=0, while the starting edge (left side edge) of the exposed electrode was located at x=1 mm.
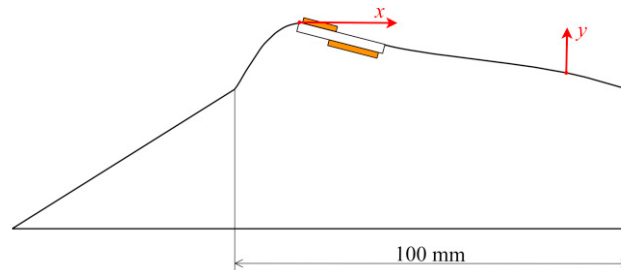

Fig. 2. Curved wall plate, reference system and actuator details.

The SDBDPA was operated by different voltage waveforms (sinus, square and triangle) generated from a function generator (Enertec Schlumberger 4431) and then amplified to HVs with a Trek Model 40/15 amplifier. The voltage waveforms were characterized by different peak-to-peak voltages ϕ_{pp} and frequency f equal to 2 kHz. An acquisition/driving card (*NI-USB 6343*) was used to externally trigger the HV amplifier. The actuator exposed electrode was connected to the output of the HV amplifier. The grounded electrode was instead connected to the ground.

Measurements of the flow velocities in presence of external flow and for both "actuator ON" and "actuator OFF" conditions were performed by using a 2-D PIV system. Simultaneously to each velocity measurement, the SDBDPA power dissipation was obtained by electrical characterization.

The applied voltage was measured with the voltage output monitor built into the amplifier (accuracy better than 0.1% of full scale). The current was instead measured by a current transformer (Bergoz Current Transformer CT-B1.0) placed in series between the grounded electrode and the ground. Both the amplifier voltage output monitor and the current transformer Bayonet Neill-Concelman (BNC) connector terminals were connected to an oscilloscope (Tektronix TDS2024C) and the respective signals were recorded with an accuracy of ±3%. This allowed to retrieve the voltage-current characteristic curves (as a function of time, t) used for the actuator power dissipation calculation. A single acquisition of the oscilloscope captured 2500 data points at a sampling rate of 25 MHz. For each input voltage, 128 single acquisitions were recorded and averaged. The mean values of the applied voltage signal ($\phi(t)$)

and of the current signal ($I(t)$) were thus obtained. In order to increase the measurement accuracy, the $\phi(t)\text{-}I(t)$ curves were saved N times throughout the duration of each PIV experiment. The mean value of the respective power dissipations was considered representative of each test case. It has to be noticed that only the data corresponding to one time period (T) were selected for the electric power dissipation calculation. This was made through an in-house algorithm implemented in Matlab, which found the time instants corresponding to two consecutive maximum values of $\phi(t)$ and discarded the values of the $\phi(t)$ and $I(t)$ signals lying outside that time interval. In definitive, the electric power dissipation $\overline{P}$ was thus calculated as follows:

$$\overline{P} = \frac{1}{N}\sum_{1}^{N}\left(\frac{1}{T}\int_{0}^{T}I(t)\phi(t)dt\right)$$ (1)

The numerical integration was performed using the trapezoidal rule and the uncertainty of each $\overline{P}$ value was estimated by standard uncertainty analysis methodology [23], resulting in at worst around ±4% (see Table 2).

The velocity measurements were taken in a streamwise plane (*x-y*) in proximity of the SDBDPA. The seeding was generated by a *Magnum 850* smoke generator (fog fluid: *Pro Smoke High Density-Martin*, characterized by a particle size of 1-1.5 μm and a particle density at room temperature of 0.95 kg/m^3). The Stokes number was evaluated. It resulted of the order 10^{-6}, indicating a good fluidic response from the tracer particles [14]. A double pulse Nd: YAG laser, EverGreen (70-200 mJ @ 532 nm), was used to generate a light sheet (~1 mm thick) at the midspan section of the curved wall plate. A FlowSense EO camera 4M with a 2048×2048 resolution was used to acquire the PIV images, spanning from *x*=-5 to *x*=53 mm (see Fig. 2 for the *x* zero position). The camera could be moved along the *x*, *y* and *z* axes by micrometer positioning stages. It was equipped with a Nikkor 60 mm f/2.8 d A/F objective (set at an aperture of 4) and an interference filter (wavelength=532 nm) to eliminate the influence of the ambient light on the recorded images. The camera was operated in double-frame mode and 1000 image pairs per run were recorded at a repetition rate of 10 Hz. Digital analysis was made using the Dantec DynamicStudio v4.10.67 software [24]. The spatial resolution of the processed PIV results was 0.5 mm. The mean velocity field was obtained by averaging the instantaneous PIV velocity maps of valid vectors.

The uncertainty on the measured *x* and *y* position in the PIV vector fields, estimated by the guidelines reported by Raffel et al. [25], was about ±0.5 mm. The uncertainty in the time-averaged velocity measurements was evaluated according to Moffat [23]. The statistical percent error in the estimation of the maximum value of the time-averaged velocity *x*-component (v_x) resulted in at worst ±0.5%. The statistical percent error in the minimum value of v_x resulted instead in at worst ±4%.

Aiming to correlate the relative jet momentum input by the SDBDPA to the flow momentum for each test case, the PIV data were used for retrieving the 2-D momentum coefficient c_μ by [11]:

$$c_\mu = J\Big/\frac{1}{2}\rho(v_{\infty,x}^{in})^2 c$$ (2)

where ρ is the fluid density and J is the steady wall-jet momentum produced immediately downstream of the actuator (*x*=20 mm is considered) , which was quantified by:

$$J = \int_{y_W}^{y_\infty} \rho(v_{x,on}^2 - v_{x,off}^2)dy$$ (3)

where, for a given *x*-coordinate, $v_{x,on}$ and $v_{x,off}$ are the time-averaged *x*-velocity profiles with and without plasma actuation. The y_W and y_∞ values are the *y*-coordinates of the profile wall and of the maximum height that we could resolve with the PIV acquisitions, respectively.

Together with the velocity fields, the PIV data were used to determine the 2-D turbulence intensity Tu in the adverse pressure gradient region. According to [1], [11], [26], the Tu was calculated by:

$$Tu\,(\%) = 100 \cdot \frac{\sqrt{\frac{1}{2}\left[\left(v_x'\big|_{rms}\right)^2 + \left(v_y'\big|_{rms}\right)^2\right]}}{v_{\infty,x}^{in}}$$ (4)

where $v_x'\big|_{rms}$ and $v_y'\big|_{rms}$ are the root-mean-square of the v_x and v_y velocity fluctuations, respectively, at each

measurement point.

2.3. Results and discussion

Table 1 reports all the studied test cases, indicating the test conditions.

Table 1. Test cases ($v_{\infty,x}^{in}$ = 3 m/s, Re=2·10^4, f =2 kHz)

Test case	Actuator state	Waveform type	ϕ_{pp} (kV)
A	OFF	-	-
B	ON	sinus	16.9±0.4
C	ON	square	17.0±0.3
D	ON	triangle	16.7±0.4

Table 2 reports, for each actuated test case, the $\overline{P}$ value, the c_μ coefficient and the c_μ coefficient "effectiveness", defined as $c_\mu / \overline{P}$. Looking at the power dissipations values, it is possible to see that the sinus and triangle waveforms had comparable dissipation powers, while the square wave implied a higher $\overline{P}$ value. Moreover, the sinus actuation also brought to the highest c_μ and $c_\mu / \overline{P}$ values; the lowest values of them were given by the square actuation.

Table 2. Actuator performances.

Test case	c_μ	$\overline{P}$ (W)	$c_\mu / \overline{P}$ (1/W)
B	0.268±0.002	4.7±0.2	0.057±0.003
C	0.223±0.002	5.9±0.2	0.038±0.002
D	0.23±0.001	4.5±0.2	0.051±0.003

Fig. 3 reports a comparison of the v_x velocity fields retrieved by PIV for all the test cases. In each iso-contour the streamlines of the velocity field are also superimposed upon the velocity distributions. It is evident that, when actuation was not present, separation was occurring in all the adverse pressure gradient area along the curved wall and a reverse flow was present in the separation region. When the actuator was switched on, the plasma generated a wall-jet [14], [27], which brought to a local acceleration of the fluid downstream in the x direction. Therefore the extension of the separation region was reduced and the magnitude of the negative velocity decreased.

Moreover, the flow angle in both the main flow and in the boundary layer was reduced by the actuation; the flow became more horizontal in the main flow and it was more attached and closer to the curved wall surface in the boundary layer [11]. Comparing the different actuation waveforms, no a substantial difference can be noticed in terms of flow control effect. However, as showed by the c_μ values results, the sinus slightly outperformed the others waveforms.
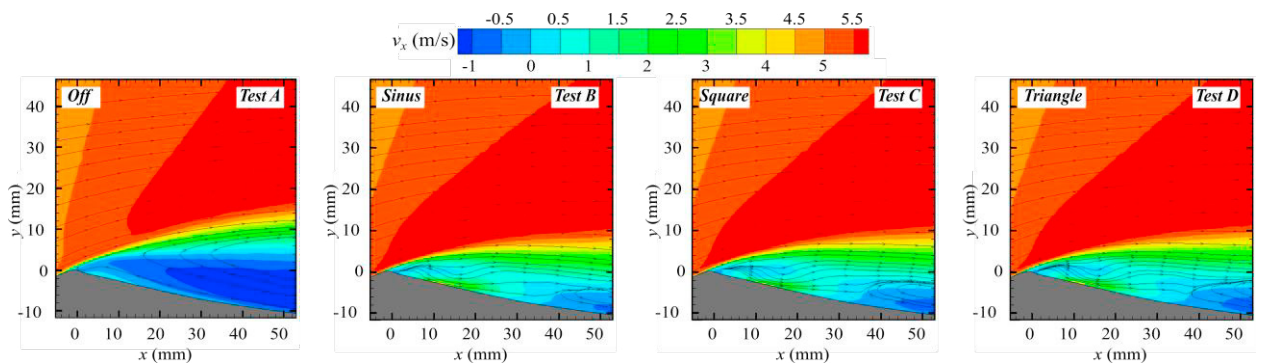

Fig. 3. PIV v_x velocity iso-contours for the different test cases.

For a more quantitative evaluation of the actuation effect, Fig. 4 reports the velocity profiles of the v_x velocity for the test cases A and B, taken over the profile at x = 20, 35 and 50 mm. It is clear that the actuator operation led to a reduction of the boundary layer thickness and of the negative velocity values.
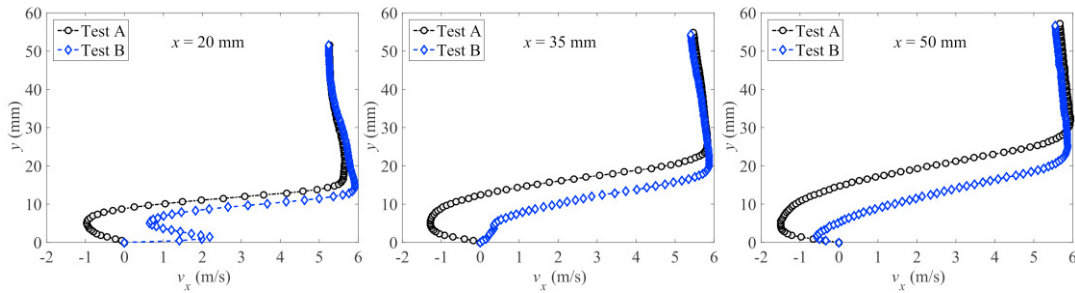
Fig. 4. PIV v_x velocity profiles taken at three different x-sections and for the actuator off case and the actuated cases with a sinus waveform.

The Tu contour maps for all the test conditions are reported in Fig. 5. In the not-actuated test cases, a wide high turbulence region was present at the boundary line between the main flow and the separated flow, starting from $x\approx10$ mm. A maximum Tu value of about 45% was reached. When the actuator was switched on, the high turbulence region moved closer to the curved wall surface. This effect was more evident for the sinus voltage excitation, which also induced slightly higher Tu values. It confirmed the observations of Bernard and Moreau [15], who found that the sinusoidal waveform enhanced the velocity fluctuations in an initially quiescent environment.
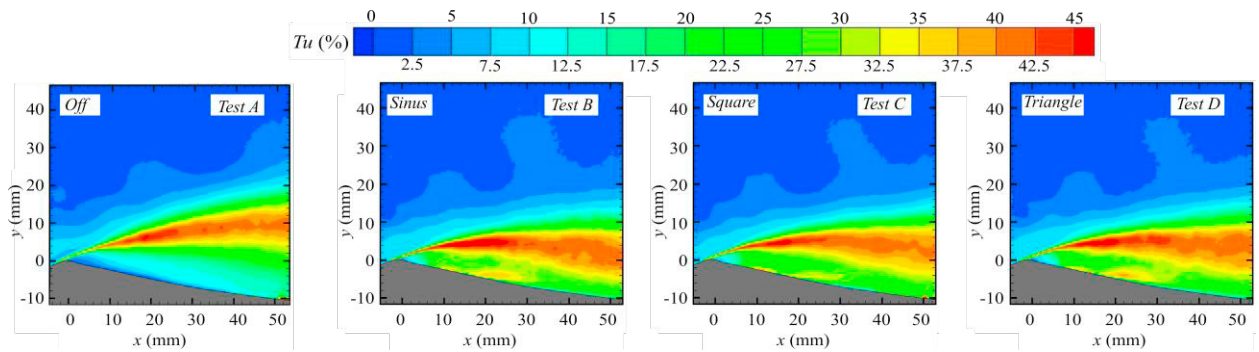

Fig. 5. PIV turbulence intensity iso-contours for the different test cases.

2.4. Conclusions

The present work investigated and compared experimentally the effect of the SDBDPA actuation voltage waveform by electrical and velocity measurements.
A curved wall profile simulating the suction surface of a LPT blade was manufactured, and the plasma flow control effect was investigated at a Re number of $2\cdot10^4$. The SDBDPA was fabricated by microfabrication techniques, involving metals thin film deposition with high manufacturing reliability control. Due to the possible device degradation in the plasma environment, an accurate materials selection was performed: Schott AF-32 glass as dielectric, while a multilayer TiN/W as electrode material.
Velocity data showed that when actuation was not present, separation was occurring in the adverse pressure gradient area along the curved wall. Moreover, a wide high turbulence region was found at the boundary line between the main flow and the separated flow. Measurements in presence of actuation demonstrated that the SDBDPA operation brought to a reduction of the separation region extension, together with the magnitude of the negative velocity values. Moreover, the flow angle in both the main flow and in the boundary layer was reduced by the active flow control effect; the flow became more horizontal in the main flow and more attached and closer to the curved wall surface in the boundary layer. The turbulence intensity results underlined that the actuator energized the boundary layer: when it was switched on, the high turbulence region moved further upstream and closer to the curved wall surface.
Comparing the different applied voltage waveforms, it was found that, at comparable peak-to-peak voltages and same excitation frequency, the sinus and triangle waveforms had comparable dissipation power, while the square wave always implied a higher $\overline{P}$ value. Moreover, the sinus brought to the highest c_μ and $c_\mu / \overline{P}$ values, while the

lowest performances were given by the square waveform actuation. The sinus, in fact, provided a separation control effect slightly higher than the one of the other voltage waveforms in terms of boundary layer thickness and negative velocities reduction in the separation region. The Tu values were also lightly larger in the sinus actuation test case.

Acknowledgements

References

[1]   T. Matsunuma and T. Segawa (2012) "Effects of Input Voltage on Flow Separation Control for Low-Pressure Turbine at Low Reynolds Number by Plasma Actuators." *Int. J. Rotating Mach*. (2012): 1–10.
[2]   D. D. Sanders, W. F. O'Brien, R. Sondergaard, M. D. Polanka, and D. C. Rabe (2010) "Predicting Separation and Transitional Flow in Turbine Blades at Low Reynolds Numbers—Part I: Development of Prediction Methodology." *J. Turbomach*. 133.3 (2010): 031011.
[3]   T. Matsunuma (2006) "Unsteady Flow Field of an Axial-Flow Turbine Rotor at a Low Reynolds Number." *J. Turbomach*. 129.2 (2006): 360-371.
[4]   J. P. Bons, R. Sondergaard, and R. B. Rivir (2002) "The Fluid Dynamics of LPT Blade Separation Control Using Pulsed Jets." *J. Turbomach*. 124.1 (2002): 77-85.
[5]   X. Wang, L. Liang, and S. Kang (2015) "Numerical Simulations on Flow Separation Within an Axial Turbine at Very Low Reynolds Number." *ASME Paper* GT2015-43108 (2015).
[6]   T. Matsunuma and Y. Tsutsui (2002) "LDV Measurements of Unsteady Flow in a Turbine Rotor." *AIAA Paper* 2002-2742 (2002).
[7]   O. P. Sharma and T. L. Butler (1987) "Predictions of Endwall Losses and Secondary Flows in Axial Flow Turbine Cascades." *J. Turbomach*. 109.2 (1987): 229-236.
[8]   J. Huang, T. C. Corke, and F. O. Thomas (2006) "Plasma Actuators for Separation Control of Low-Pressure Turbine Blades." *AIAA J*. 44.1 (2006): 51–57.
[9]   S. I. Benton, C. Bernardini, J. P. Bons, and R. Sondergaard (2014) "Parametric Optimization of Unsteady End Wall Blowing on a Highly Loaded Low-Pressure Turbine." *J. Turbomach*. 136.7 (2014): 071013.
[10]   M. J. Bloxham and J. P. Bons (2010) "Combined Blowing and Suction to Control Both Midspan and Endwall Losses in a Turbomachinery Passage." *ASME Paper* GT2010-23552 (2010).
[11]   E. Pescini, F. Marra, M. G. De Giorgi, L. Francioso, and A. Ficarella (2016) "Investigation of the boundary layer characteristics for assessing the DBD plasma actuator control of the separated flow at low Reynolds numbers." *Exp. Therm. Fluid Sci*. 81 (2016): 482-498.
[12]   D. Burman, T. W. Simon, U. Kortshagen, and D. Ernie (2011) "Separation Control Using Plasma Actuators: Steady Flow in Low Pressure Turbines." *ASME Paper* GT2011-46807 (2011).
[13]   D. P. Rizzetta and M. R. Visbal (2007) "Numerical Investigation of Plasma-Based Flow Control for Transitional Highly-Loaded Low-Pressure Turbine." *AIAA J*. 45.10 (2007): 2554–2564.
[14]   E. Pescini, L. Francioso, M. G. De Giorgi, and A. Ficarella (2015) "Investigation of a Micro Dielectric Barrier Discharge Plasma Actuator for Regional Aircraft Active Flow Control." *IEEE Trans. Plasma Sci*. 43.10 (2015): 3668–3680.
[15]   N. Benard and E. Moreau (2012) "Role of the electric waveform supplying a dielectric barrier discharge plasma actuator." *Appl. Phys. Lett*. 100.19 (2012): 193503.
[16]   J. Jolibois and E. Moreau (2009) "Enhancement of the Electromechanical Performances of a Single Dielectric Barrier Discharge Actuator." *IEEE Trans. Dielectr. Electr. Insul*. 16.3 (2009): 758–767.
[17]   F. O. Thomas, T. C. Corke, M. Iqbal, A. Kozlov, and D. Schatzman (2009) "Optimization of Dielectric Barrier Discharge Plasma Actuators for Active Aerodynamic Flow Control." *AIAA J*. 47.9 (2009): 2169–2178.
[18]   M. Kotsonis and S. Ghaemi (2012) "Performance improvement of plasma actuators using asymmetric high voltage waveforms." J. *Phys. Appl. Phys*. 45.4 (2012): 045204.
[19]   T. Matsunuma, H. Abe, and Y. Tsutsui (2002) "LDV Measurements of Unsteady Flow within a Turbine Rotor at Low Reynolds Numbers." *JSME Int. J. Ser. B* 45.3 (2002): 457–464.
[20]   T. Matsunuma and Y. Tsutsui (2005) "Effects of Low Reynolds Number on Wake-Generated Unsteady Flow of an Axial-Flow Turbine Rotor." *Int. J. Rotating Mach*. 2005.1 (2005): 1–15.
[21]   E. Pescini, M. G. De Giorgi, L. Francioso, A. Taurino, M. C. Martucci, and P. Lavoie (2016) "Electrode Material Degradation Monitoring for Durable Dielectric Barrier Discharge Plasma Actuators Manufacturing." *AIAA Paper* 2016-0196 (2016).
[22]   N. M. Houser, L. Gimeno, R. E. Hanson, T. Goldhawk, T. Simpson, and P. Lavoie (2013) "Microfabrication of dielectric barrier discharge plasma actuators for flow control." *Sens. Actuators Phys*. 201 (2013): 101–104.
[23]   R. J. Moffat (1988) "Describing the uncertainties in experimental results." *Exp. Therm. Fluid Sci*. 1.1 (1988): 3–17.
[24]   Dantec Dynamics A/S (2014) *DynamicStudio User's Guide V4.10*, DK–2740 Skovlunde, Denmark: Chap. 15.
[25]   M. Raffel, C. E. Willert, and J. Kompenhans (1998) *Particle image velocimetry: a practical guide*, Springer-verlag Berlin Heidelberg.
[26]   P. Mycek, B. Gaurier, G. Germain, G. Pinon, and E. Rivoalen (2014) "Experimental study of the turbulence intensity effects on marine current turbines behaviour. Part I: One single turbine." *Renew. Energy* 66 (2014): 729–746.
[27]   E. Pescini, D. S. Martínez, M. G. D. Giorgi, and A. Ficarella (2015) "Optimization of micro single dielectric barrier discharge plasma actuator models based on experimental velocity and body force fields." *Acta Astronaut*. 116 (2015): 318–332.